




# Cosmogenic background simulations for neutrinoless double beta decay with the DARWIN observatory at various underground sites

DARWIN Collaboration\*

M. Adrover<sup>1</sup>, L. Althueser<sup>2</sup>, B. Andrieu<sup>3</sup>, E. Angelino<sup>4</sup>, J. R. Angevaere<sup>5</sup>, B. Antunovic<sup>6,b</sup>, E. Aprile<sup>7</sup>, M. Babicz<sup>1</sup>, D. Bajpai<sup>9</sup>, E. Barberio<sup>11</sup>, L. Baudis<sup>1</sup>, M. Bazyk<sup>12</sup>, N. Bell<sup>11</sup>, L. Bellagamba<sup>13</sup>, R. Biondi<sup>14</sup>, Y. Biondi<sup>15</sup>, A. Bismark<sup>1</sup>, C. Boehm<sup>16</sup>, A. Breskin<sup>17</sup>, E. J. Brookes<sup>5</sup>, A. Brown<sup>18</sup>, G. Bruno<sup>8</sup>, R. Budnik<sup>17</sup>, C. Capelli<sup>1</sup>, J. M. R. Cardoso<sup>19</sup>, A. Chauvin<sup>20</sup>, A. P. Cimental Chavez<sup>1</sup>, A. P. Colijn<sup>5</sup>, J. Conrad<sup>21</sup>, J. J. Cuenca-García<sup>1,15,a</sup> , V. D'Andrea<sup>22,c</sup>, M. P. Decowski<sup>5</sup>, A. Deisting<sup>23</sup>, P. Di Gangi<sup>13</sup>, S. Diglio<sup>12</sup>, M. Doerenkamp<sup>20</sup>, G. Drexlin<sup>24</sup>, K. Eitel<sup>15</sup>, A. Elykov<sup>15</sup>, R. Engel<sup>15</sup>, S. Farrell<sup>25</sup>, A. D. Ferella<sup>26</sup>, C. Ferrari<sup>22</sup>, H. Fischer<sup>18</sup>, M. Flierman<sup>5</sup>, W. Fulgione<sup>22</sup>, P. Gaemers<sup>5</sup>, R. Gaior<sup>3</sup>, M. Galloway<sup>1</sup>, N. Garroum<sup>3</sup>, S. Ghosh<sup>27</sup>, F. Girard<sup>3</sup>, R. Glade-Beucke<sup>18</sup>, F. Glück<sup>15</sup>, L. Grandi<sup>28</sup>, J. Grigat<sup>18</sup>, R. Gröble<sup>15</sup>, H. Guan<sup>27</sup>, M. Guida<sup>14</sup>, R. Hammann<sup>14</sup>, V. Hannen<sup>2</sup>, S. Hansmann-Menzemer<sup>20</sup>, N. Hargittai<sup>17</sup>, T. Hasegawa<sup>29</sup>, C. Hils<sup>23</sup>, A. Higuera<sup>25</sup>, K. Hiraoka<sup>29</sup>, L. Hoetzsch<sup>14</sup>, M. Iacovacci<sup>31</sup>, Y. Itow<sup>29</sup>, J. Jakob<sup>2</sup>, F. Jörg<sup>14</sup>, M. Kara<sup>15</sup>, P. Kavargin<sup>17</sup>, S. Kazama<sup>29</sup>, M. Keller<sup>20</sup>, B. Kilminster<sup>1</sup>, M. Kleifges<sup>10</sup>, M. Kobayashi<sup>29</sup>, A. Kopec<sup>31</sup>, B. von Krosigk<sup>32</sup>, F. Kuger<sup>18</sup>, H. Landsman<sup>17</sup>, R. F. Lang<sup>27</sup>, I. Li<sup>25</sup>, S. Li<sup>27</sup>, S. Liang<sup>25</sup>, S. Lindemann<sup>18</sup>, M. Lindner<sup>14</sup>, F. Lombardi<sup>23</sup>, J. Loizeau<sup>12</sup>, T. Luce<sup>18</sup>, Y. Ma<sup>31</sup>, C. Macolino<sup>26</sup>, J. Mahlstedt<sup>21</sup>, A. Mancuso<sup>13</sup>, T. Marrodán Undagoitia<sup>14</sup>, J. A. M. Lopes<sup>19,d</sup>, F. Marignetti<sup>30</sup>, K. Martens<sup>33</sup>, J. Masbou<sup>12</sup>, S. Mastroianni<sup>30</sup>, S. Milutinovic<sup>6</sup>, K. Miuchi<sup>34</sup>, R. Miyata<sup>29</sup>, A. Molinaro<sup>4</sup>, C. M. B. Monteiro<sup>19</sup>, K. Morá<sup>7</sup>, E. Morteau<sup>12</sup>, Y. Mosbacher<sup>17</sup>, J. Müller<sup>18</sup>, M. Murra<sup>7</sup>, J. L. Newstead<sup>11</sup>, K. Ni<sup>31</sup>, U. G. Oberlack<sup>23</sup>, I. Ostrovskiy<sup>9</sup>, B. Paetsch<sup>17</sup>, M. Pandurovic<sup>6</sup>, Q. Pellegrini<sup>3</sup>, R. Peres<sup>1</sup>, J. Pienaar<sup>28</sup>, M. Pierre<sup>5</sup>, M. Piottter<sup>14</sup>, G. Plante<sup>7</sup>, T. R. Pollmann<sup>5</sup>, L. Principe<sup>12</sup>, J. Qi<sup>31</sup>, J. Qin<sup>27</sup>, M. Rajado Silva<sup>1</sup>, D. Ramírez García<sup>1</sup>, A. Razeto<sup>22</sup>, S. Sakamoto<sup>29</sup>, L. Sanchez<sup>25</sup>, P. Sanchez-Lucas<sup>1,e</sup>, J. M. F. dos Santos<sup>19</sup>, G. Sartorelli<sup>13</sup>, A. Scaffidi<sup>35</sup>, P. Schulte<sup>2</sup>, H.-C. Schultz-Coulon<sup>32</sup>, H. Schulze Eifing<sup>2</sup>, M. Schumann<sup>18</sup>, L. Scotto Lavina<sup>3</sup>, M. Selvi<sup>13</sup>, F. Semeria<sup>13</sup>, P. Shagin<sup>23</sup>, S. Sharma<sup>20</sup>, W. Shen<sup>20</sup>, M. Silva<sup>19</sup>, H. Simgen<sup>14</sup>, R. Singh<sup>27</sup>, M. Solmaz<sup>24</sup>, O. Stanley<sup>11</sup>, M. Steidl<sup>15</sup>, P.-L. Tan<sup>21</sup>, A. Terliuk<sup>20</sup>, D. Thers<sup>12</sup>, T. Thümmel<sup>15</sup>, F. Tönnies<sup>18</sup>, F. Toschi<sup>15</sup>, G. Trincherro<sup>4</sup>, R. Trotta<sup>35</sup>, C. Tunnell<sup>25</sup>, P. Urquijo<sup>11</sup>, K. Valerius<sup>15</sup>, S. Vecchi<sup>36</sup>, S. Vetter<sup>15</sup>, G. Volta<sup>1</sup>, D. Vorkapic<sup>6</sup>, W. Wang<sup>9</sup>, K. M. Weerman<sup>5</sup>, C. Weinheimer<sup>2</sup>, M. Weiss<sup>17</sup>, D. Wenz<sup>2,23</sup>, C. Wittweg<sup>1</sup>, J. Wolf<sup>24</sup>, T. Wolf<sup>14</sup>, V. H. S. Wu<sup>15</sup>, M. Wurm<sup>23</sup>, Y. Xing<sup>12</sup>, M. Yamashita<sup>33</sup>, J. Ye<sup>7</sup>, G. Zavattini<sup>36</sup>, K. Zuber<sup>37</sup>

<sup>1</sup> Physik-Institut, University of Zürich, 8057 Zurich, Switzerland

<sup>2</sup> Institut für Kernphysik, Westfälische Wilhelms-Universität Münster, 48149 Münster, Germany

<sup>3</sup> LPNHE, Sorbonne Université, CNRS/IN2P3, 75005 Paris, France

<sup>4</sup> INAF-Astrophysical Observatory of Torino, Department of Physics, University of Torino and INFN-Torino, 10125 Turin, Italy

<sup>5</sup> Nikhef and the University of Amsterdam, Science Park, 1098XG Amsterdam, The Netherlands

<sup>6</sup> Vinca Institute of Nuclear Science, University of Belgrade, Mihajla Petrovica Alasa 12-14, Belgrade, Serbia

<sup>7</sup> Physics Department, Columbia University, New York, NY 10027, USA

<sup>8</sup> New York University Abu Dhabi-Center for Astro, Particle and Planetary Physics, Abu Dhabi, United Arab Emirates

<sup>9</sup> Department of Physics and Astronomy, University of Alabama, Tuscaloosa, AL 35487, USA

<sup>10</sup> Institute for Data Processing and Electronics, Karlsruhe Institute of Technology, 76021 Karlsruhe, Germany

<sup>11</sup> ARC Centre of Excellence for Dark Matter Particle Physics, School of Physics, The University of Melbourne, Melbourne, VIC 3010, Australia

<sup>12</sup> SUBATECH, IMT Atlantique, CNRS/IN2P3, Université de Nantes, 44307 Nantes, France

<sup>13</sup> Department of Physics and Astronomy, University of Bologna and INFN-Bologna, 40126 Bologna, Italy

<sup>14</sup> Max-Planck-Institut für Kernphysik, 69117 Heidelberg, Germany

<sup>15</sup> Institute for Astroparticle Physics, Karlsruhe Institute of Technology, 76021 Karlsruhe, Germany

<sup>16</sup> School of Physics, The University of Sydney, Camperdown, Sydney, NSW 2006, Australia

<sup>17</sup> Department of Particle Physics and Astrophysics, Weizmann Institute of Science, 7610001 Rehovot, Israel

<sup>18</sup> Physikalisches Institut, Universität Freiburg, 79104 Freiburg, Germany

<sup>19</sup> LIBPhys, Department of Physics, University of Coimbra, 3004-516 Coimbra, Portugal

<sup>20</sup> Physikalisches Institut, Universität Heidelberg, Heidelberg, Germany

<sup>21</sup> Department of Physics, Oskar Klein Centre, Stockholm University, AlbaNova, 10691 Stockholm, Sweden

<sup>22</sup> INFN-Laboratori Nazionali del Gran Sasso and Gran Sasso Science Institute, 67100 L'Aquila, Italy

<sup>23</sup> Institut für Physik and Exzellenzcluster PRISMA+, Johannes Gutenberg-Universität Mainz, 55099 Mainz, Germany

- <sup>24</sup> Institute of Experimental Particle Physics, Karlsruhe Institute of Technology, 76021 Karlsruhe, Germany
- <sup>25</sup> Department of Physics and Astronomy, Rice University, Houston, TX 77005, USA
- <sup>26</sup> Department of Physics and Chemistry, University of L'Aquila, 67100 L'Aquila, Italy
- <sup>27</sup> Department of Physics and Astronomy, Purdue University, West Lafayette, IN 47907, USA
- <sup>28</sup> Department of Physics and Kavli Institute for Cosmological Physics, University of Chicago, Chicago, IL 60637, USA
- <sup>29</sup> Kobayashi-Maskawa Institute for the Origin of Particles and the Universe, and Institute for Space-Earth Environmental Research, Nagoya University, Furo-cho, Chikusa-ku, Nagoya, Aichi 464-8602, Japan
- <sup>30</sup> Department of Physics "Ettore Pancini", University of Napoli and INFN-Napoli, 80126 Naples, Italy
- <sup>31</sup> Department of Physics, University of California San Diego, La Jolla, CA 92093, USA
- <sup>32</sup> Kirchhoff-Institut für Physik, Universität Heidelberg, Heidelberg, Germany
- <sup>33</sup> Kavli Institute for the Physics and Mathematics of the Universe (WPI), The University of Tokyo, Higashi-Mozumi, Kamioka, Hida, Gifu 506-1205, Japan
- <sup>34</sup> Department of Physics, Kobe University, Kobe, Hyogo 657-8501, Japan
- <sup>35</sup> Theoretical and Scientific Data Science, Scuola Internazionale Superiore di Studi Avanzati (SISSA), 34136 Trieste, Italy
- <sup>36</sup> INFN-Ferrara and Dip. di Fisica e Scienze della Terra, Università di Ferrara, 44122 Ferrara, Italy
- <sup>37</sup> Technische Universität Dresden, 01069 Dresden, Germany

Received: 29 June 2023 / Accepted: 27 November 2023 / Published online: 27 January 2024

© The Author(s) 2024

**Abstract** Xenon dual-phase time projections chambers (TPCs) have proven to be a successful technology in studying physical phenomena that require low-background conditions. With 40 t of liquid xenon (LXe) in the TPC baseline design, DARWIN will have a high sensitivity for the detection of particle dark matter, neutrinoless double beta decay ( $0\nu\beta\beta$ ), and axion-like particles (ALPs). Although cosmic muons are a source of background that cannot be entirely eliminated, they may be greatly diminished by placing the detector deep underground. In this study, we used Monte Carlo simulations to model the cosmogenic background expected for the DARWIN observatory at four underground laboratories: Laboratori Nazionali del Gran Sasso (LNGS), Sanford Underground Research Facility (SURF), Laboratoire Souterrain de Modane (LSM) and SNOLAB. We present here the results of simulations performed to determine the production rate of  $^{137}\text{Xe}$ , the most crucial isotope in the search for  $0\nu\beta\beta$  of  $^{136}\text{Xe}$ . Additionally, we explore the contribution that other muon-induced spallation products, such as other unstable xenon isotopes and tritium, may have on the cosmogenic background.

## 1 Introduction

Dual-phase xenon TPCs hold the best constraints for direct detection of weakly interacting massive particles (WIMPs) for masses above  $6 \text{ GeV}/c^2$  [1, 2], and they have increased the current sensitivity with their upgraded versions [3–5]. Likewise, experiments using xenon in its pure form or dissolved in a liquid scintillator provide competitive limits on the half-life of the neutrinoless double beta decay of  $^{136}\text{Xe}$  [6–8], with plans to probe half-lives up to two orders of magnitude larger in future and upgraded versions of these experiments [9–11]. The latest achievements in background mitigation, together with the increase of the target masses, have demonstrated that xenon experiments, and in particular xenon TPCs, are powerful instruments for other rare-event searches as well. This includes the observation of the extremely rare decay of  $^{124}\text{Xe}$  via double electron capture [12], the search for solar neutrino interactions on nuclei [13], and searches for solar axions, axion-like particles and dark photons [14, 15].

DARWIN, a proposed next-generation xenon experiment, will push the sensitivity to all these phenomena even further [16–18]. In its baseline design, DARWIN will use 40 t of instrumented liquid xenon in a dual-phase xenon TPC to complete an extensive science program. To fully exploit the physics goals of DARWIN an unprecedented, ultra-low background level will be required. To achieve such a level, external radiogenic backgrounds from detector materials as well as the concentration of  $^{222}\text{Rn}$ , which emanates from detector components, have to be reduced to negligible contributions. With this, cosmogenic background may become an important contribution for the  $0\nu\beta\beta$  search if other relevant backgrounds, with the exception of the neutrino background, are reduced to a negligible level.

Even though the detectors are placed deep underground to shield them from cosmic radiation, muons with an energy

\* e-mail: [darwin-pub@darwin-observatory.org](mailto:darwin-pub@darwin-observatory.org)

<sup>a</sup> e-mail: [jose.cuenca@physik.uzh.ch](mailto:jose.cuenca@physik.uzh.ch)

<sup>b</sup> Also at University of Banja Luka, 78000 Banja Luka, Bosnia and Herzegovina

<sup>c</sup> Also at INFN-Roma Tre, 00146 Rome, Italy

<sup>d</sup> Also at Coimbra Polytechnic-ISEC, 3030-199 Coimbra, Portugal

<sup>e</sup> Also at University of Granada, Granada, Spain

<sup>f</sup> Also at Max-Planck-Institut für Kernphysik, 69117 Heidelberg, Germany

$\mathcal{O}(1 \text{ TeV})$  can penetrate several kilometers of rock, concrete and shielding materials and reach the detector, producing a considerable amount of secondary neutrons through hadronic and electromagnetic showers that can potentially mimic a WIMP nuclear recoil interaction. These muon-induced neutrons can also produce long-lived radionuclides via different processes, such as inelastic interactions or captures. Radionuclides produced in the xenon volume as a consequence of these processes are a constant and irreducible source of background events in a wide energy range that can turn dominant if all the other background contributions are negligible. Additional veto systems, such as muon-veto water-filled tanks (Sect. 2.2), although not perfect at suppressing certain backgrounds, such as neutrons, would help in identifying muon-induced events. Moreover, activation of the xenon above ground during production, storage and transportation, can be problematic too [19]. However, this can be mitigated by taking proper actions before construction and filling of the detector.

One of the most significant contributions to the background in neutrinoless double beta decay experiments using xenon detectors is the decay of  $^{137}\text{Xe}$  which is produced after a neutron is captured by  $^{136}\text{Xe}$ . This isotope  $\beta$ -decays to  $^{137}\text{Cs}$  with a  $Q_\beta$  of 4.162 MeV while the neutrinoless double beta decay of  $^{136}\text{Xe}$  has a  $Q_{\beta\beta}$  of 2.458 MeV. Since the electrons produced in the  $^{137}\text{Xe}$  decay have a continuous energy spectrum, they can potentially mimic the signal of a neutrinoless double beta decay, therefore reducing the sensitivity of the detector to this process. Experiments devoted to the neutrinoless double beta decay searches using  $^{136}\text{Xe}$ , such as nEXO, KamLAND-Zen or NEXT have estimated a significant  $^{137}\text{Xe}$  background [9, 20, 21].

For the cosmogenic activation during operation, the depth of the underground laboratory becomes a crucial factor: the deeper the experimental site, the lower the muon flux, but, at the same time, the higher the mean energy of the muons and of their induced secondary particles. Given that the underground location of the DARWIN experiment is still to be decided, the study of the production of cosmogenic backgrounds at different sites will inform this choice.

An accurate evaluation of the cosmogenic background requires realistic simulations. Using several already existing simulation packages, we developed a framework to perform full Monte Carlo simulations with muons at several underground locations. This represents an improvement compared to our previous work on the simulation of the neutrinoless double beta decay background [18]. Here, we introduce the various elements that were implemented to expand upon the aforementioned study.

This work is organized as follows: In Sect. 2 we describe the simulation framework. Section 3.1 focuses on the most problematic and abundant particles produced due to muon interactions, the muon-induced neutrons. In Sects. 3.2 and 3.3

we discuss the production of two radionuclides that can affect the sensitivity of DARWIN to different physics channels. Finally, we discuss and summarize the main results of our simulations in Sect. 4.

## 2 The DARWIN-Geant4 simulation framework

The transport code Geant4 [22] is one of the most robust simulation tools currently available and its use is very common in high energy physics. We have developed the DARWIN-Geant4 software package to perform the entire set of simulations for our detector. This framework is constructed using the libraries distributed with the 10.6.p02 version of Geant4.

In the next subsections, we enumerate the geometry components that make up the DARWIN experiment (Sects. 2.1, 2.2, 2.3). This includes the shielding materials of the experimental hall (rock and concrete) together with the veto systems and the TPC. Then, we list the set of physics processes that were used in these simulation (Sect. 2.4). Finally, we describe the working principle of the muon generator tool and how it is adapted to the different underground locations (Sect. 2.5)

### 2.1 Simulation of the experimental hall

Each site considered in this study has advantages and disadvantages that must be addressed, regarding not only physics but also logistics, etc. For this work, the parameters that we considered relevant were the size of the experimental hall, the measured total muon flux, the mean energy (that is related to the depth of the site) and the angular distribution of the incident muons. In Fig. 1 the measured total muon flux as a function of the depth for several underground laboratories is shown.

Some of these laboratories have several experimental halls that could be potentially available. However, since other experiments are underway, we have selected those halls that can be best adapted to the size of the DARWIN baseline design and according to our scheduled timeline. Based on the size of the hall, the number and size of components in the experimental setup may be reduced or modified, especially in the case of the muon veto system (Sect. 2.2). The four laboratories that were considered in this study are LNGS, SURE, LSM and SNOLAB. In order to perform a realistic simulation, we have implemented the geometry of the experimental halls in our simulation framework using the technical drawings provided by the laboratories.

Since all these facilities are shielded by several kilometers of rock, it is necessary to determine how much surrounding material needs to be simulated. To ensure an equilibrium between the secondary particles production and muon fluxes,

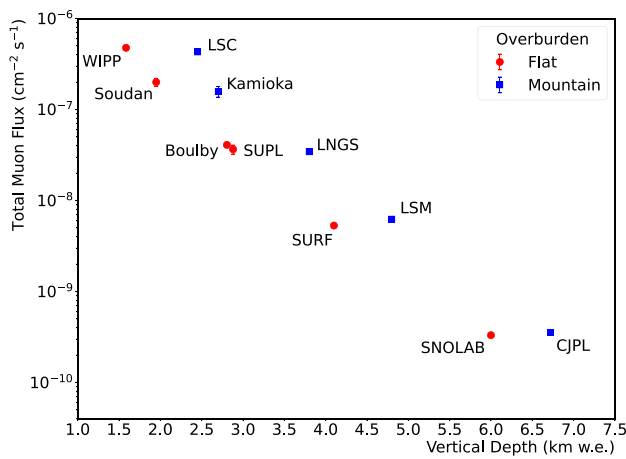


**Fig. 1** Total muon flux for several underground laboratories as a function of the depth in kilometers water equivalent (km w.e.). The data points correspond to: Waste Isolation Pilot Plant (WIPP) [23], Canfranc Underground Laboratory (LSC) [24], Soudan Underground Laboratory [25], Kamioka Observatory [26], Boulby Underground Laboratory [27], Stawell Underground Physics Laboratory (SUPL) [28], Laboratori Nazionali del Gran Sasso (LNGS) [29], Sanford Underground Research Facility (SURF) [30], Modane Underground Laboratory (LSM) [31], SNOLAB [32], China Jinping Underground Laboratory (CJPL) [33]

we used 5 m of rock for the walls of the halls. This value has been shown in previous cosmogenic simulations to be sufficient to achieve this equilibrium [34], and we used it in all four locations of this study. Besides the rock, other shielding materials, such as concrete, may be also present. The additional layers of concrete were simulated following the specifications indicated by the technical drawings.

We now briefly describe the four laboratories, including the values of the geometrical parameters that were implemented in our simulation framework.

### LNGS

Laboratori Nazionali del Gran Sasso (LNGS) are located in Italy and hosts, among others, the XENONnT dark matter experiment. It has three main experimental halls and for these simulations, we have implemented Hall B. Its  $xy$ -projection is a rectangle of 18.2 m  $\times$  60.0 m and the ceiling is a cylindrical vault with a maximum height of 20 m. The inner part of the hall is covered with a layer of concrete of 50 cm thickness. The chemical composition that we implemented in the code for the rock and concrete materials is defined in [35].

### SURF

Sanford Underground Research Facility (SURF) is a former gold mine located in South Dakota and currently is hosting the LZ dark matter experiment. In our code, we simulated the Davis cavern as a box of 17 m ( $l$ )  $\times$  10 m ( $w$ )  $\times$  12 m ( $h$ ). It has no concrete layer, and therefore the entire hall is made of rock. The chemical composition of the SURF rock is imple-

mented as in [36]. Recently there has been funding approved to create additional space at the underground facility. This new space will be much larger than the Davis cavern simulated in this work.

### LSM

In France, Laboratoire Souterrain de Modane (LSM) has also hosted dark matter experiments such as EDELWEISS. The only available place is the Grand Hall, with an area of 10 m  $\times$  20 m. The ceiling is an elliptical dome that provides a maximum height of approximately 17 m. The inner part of the hall is covered by a 30 cm layer of concrete. The chemical composition of rock and concrete was implemented as in [37].

### SNOLAB

The deepest location considered in this study is SNOLAB. It is located in Canada and in the future it will host the SuperCDMS dark matter experiment. For this work, we simulated the Cube hall. It is a box 18 m ( $l$ )  $\times$  15 m ( $w$ )  $\times$  20 m ( $h$ ). For the shielding materials we used the composition in the SNOLAB reference manual [38].

## 2.2 The muon veto system

In the DARWIN baseline design, the LXe TPC is located inside of a water tank that serves as water-Cherenkov muon veto. This water tank is implemented here as a 0.5 cm thick stainless steel cylinder with a truncated cone on top filled with water. For the cylinder of radius  $R$  and height  $h$ , the top cone has a height of  $h/5$  and a top radius of  $R/4$ . As an example, Fig. 6 (turquoise region) shows the water tank proposed for the hall B at LNGS. There, the main body consists of a cylinder of 10 m height, and a cone with the same radius of the cylinder but truncated at 2 m is attached to it at  $z = 5$  m.

In the baseline design, the water tank has a radius of 6 m. However, a tank of this size does not fit in all underground locations of this study. We adapted the size of the tank where necessary while preserving its aspect, as indicated in Table 1.

**Table 1** Summary of the geometrical parameters implemented for the underground laboratories of this study. The second column shows the names of the experimental hall, together with the shape of the ceiling (third column). Fourth and fifth columns show the radius and total height of the water tank simulated for each hall

Site	Hall	Shape	$R_{wt}$ (m)	$h_{wt}$ (m)
LNGS	B	Vault	6	12.0
SURF	Davis Cavern	Box	4	9.6
LSM	Grand Hall	Vault	4	9.6
SNOLAB	Cube Hall	Box	6	14.4



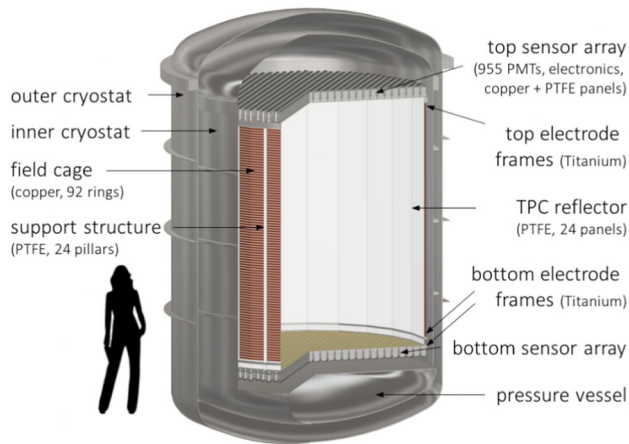


**Fig. 2** Schematic overview of the DARWIN geometry implemented in the DARWIN-Geant4 framework. It consists of a cylindrical TPC, with two sensor arrays, electrodes and field shaping rings surrounding the active volume. The TPC is placed inside a double walled cryostat made of titanium

Despite having adjusted the size of the water tank to make it as close to reality as possible, for laboratories like LSM and the current SURF, it may prove too small when considering other physical processes. It is possible that for the observables proposed in this study, the tank size may not be relevant, but it could be if we consider gamma rays from rock or other background sources.

### 2.3 The DARWIN cryostat and TPC

For the simulations, we have used the same detector geometry as implemented in [18]. In the baseline design, the DARWIN TPC consists of a cylindrical dual-phase TPC with a diameter and height of 2.6 m (aspect ratio 1:1), see Fig. 2. It has two photosensor arrays (on top and bottom) formed by 995 R11410-21 Hamamatsu photomultiplier tubes (PMTs) [39]. The PMTs are held in place by polytetrafluoroethylene (PTFE) and copper disks. The lateral part of the cylinder is fully covered with PTFE reflector panels and 24 supporting PTFE pillars. The detector is equipped with a set of electrodes and 92 copper field cage surrounding the TPC.

The TPC is placed inside a double-walled vacuum insulated cryostat with a wall thickness of 5 mm made of titanium. The vessels are simulated as cylindrical bodies finished with torus-spherical domes (DIN 28011 [40]) on top and bottom. Stiffener rings are also added to the design in order to prevent deformations of the vessel due to the pressure. Additionally, a filler vessel, consisting of a metallic shell filled with pressurized gas, is positioned in the bottom dome to yield a flat bottom surface and minimize the liquid xenon filling mass.

The active volume is filled with a total mass of 40 t of natural liquid xenon together with 30 kg of gaseous xenon on the top part of the TPC and the upper dome. For the simulation

**Table 2** Natural abundance of xenon isotopes used in these simulations. The values are given by the Geant4 internal material database (NIST)

Isotope	Abundance (%)
$^{124}\text{Xe}$	0.09
$^{126}\text{Xe}$	0.09
$^{128}\text{Xe}$	1.92
$^{129}\text{Xe}$	26.44
$^{130}\text{Xe}$	4.08
$^{131}\text{Xe}$	21.18
$^{132}\text{Xe}$	26.89
$^{134}\text{Xe}$	10.44
$^{136}\text{Xe}$	8.87

of the active xenon material, we have used the isotopic composition of natural xenon provided by the Geant4 material database. The mixture, together with the abundance of each isotope, is detailed in Table 2.

### 2.4 Geant4 physics lists

The Geant4 toolkit distributes a set of physics lists that are maintained and updated with each version. A full detailed description of these physics lists can be found in the Geant4 physics reference manual [41], together with their recommended usage.

We incorporated the modular nature of Geant4 in our simulation framework, which allows the user to create custom physics lists. We have carried out a systematic study of the features and consistency of several of them by means of toy Monte Carlo simulations. These simulations had a very simplified geometry formed by a rectangular block of rock of 5 m thickness and a cylinder of 2 m radius, 2 m height filled with liquid xenon. The primary particles were vertical muons with fixed energy of 300 GeV. As control parameters, we have chosen the muon-induced neutrons produced in the rock and the  $^{137}\text{Xe}$  production rate.

The physics lists that we used in these toy simulations were implemented in two different ways: *pure* and *mixed* configurations. In the pure version, we used the physics lists as they are distributed with our Geant4 release. In this configuration, we tested the *Shielding*, *ShieldingLEND*, *QGSP\_BIC\_HP* and *QGSP\_BERT\_HP* lists. For the mixed configurations, we use the *emlivermore* physics list for the electromagnetic processes, while for the hadronic interactions we used the hadronic part of the *Shielding*, *ShieldingLEND*, *QGSP\_BIC\_HP* and *QGSP\_BERT\_HP* physics lists. These physics lists have been validated in simulations of experiments placed underground, being the *Shielding* list the recommended by the Geant4 developers in these type of simulations. The *ShieldingLEND* list is a flavour of *Shielding* that uses the Low-Energy

**Table 3** Mean values of the energy and angles (direction) of the primary muons produced with the MUSUN software for the underground locations considered in this study. The right column shows the density of the shielding rock used in MUSUN and in our Geant4 code

Site	$\langle E_\mu \rangle$ (GeV)	$\langle \theta \rangle$ ( $^\circ$ )	$\langle \Phi \rangle$ ( $^\circ$ )	$\langle \rho \rangle$ ( $\text{g cm}^{-3}$ )
LNGS	272.7	37.42	200.90	2.71
SURF	284.7	27.09	170.38	2.70
LSM	301.3	37.55	169.90	2.65
SNOLAB	309.6	24.69	179.96	2.83

Nuclear Database (LEND) database to describe the transport of low-energy neutrons.

The results produced by the toy simulations did not show a significant discrepancy in the values of the control parameters. All results were of the same order of magnitude and they were compatible within 30% in the  $^{137}\text{Xe}$  production rate. We attribute this to the difference between the models implemented in the physics lists. Even though the pure configurations produced similar results as the mixed, the computational time of the second is significantly larger than the first. In this set of toy simulations, we estimated that simulations using the pure configurations are  $\sim 20\%$  faster.

Therefore, we decided to perform the full simulations using the pure `Shielding` as the main list together with the pure `ShieldingLEND` and `QGSP_BIC_HP` lists as control simulations.

## 2.5 The primary muon generator

We used the MUSIC-MUSUN software [42] to obtain the kinematic information of muons that serves as input to a custom muon generator in Geant4. With this software it is possible to simulate the energy-direction correlation of the muons at each underground facility taking into account parameters such as rock density or the orography of the lab. The input consists of a mixture of  $\mu^+$  and  $\mu^-$  muons with a ratio of  $\mu^+/\mu^- = 1.3$  in their populations. A summary of the properties of the primary muons is found in Table 3.

For each event, the generator reads a line of the MUSUN file containing the muon-type ( $\mu^+$  or  $\mu^-$ ), its energy and the direction of propagation. The position of the primary vertex is found using a three-step algorithm that we call *random sampling-rotation-projection*. In this algorithm we use a disk of radius  $R$  centred at the origin of the coordinate system, which is set at the center of the TPC. This algorithm, is analogous to the sampling methods used in [34,37] and works as follows:

**Table 4** Measured muon fluxes,  $\phi \pm \sigma(\phi)$ , for the underground laboratories considered in this study. The third column shows the radius of the disk used in the muon generator and the last column is the equivalent live-time

Site	Muon flux ( $\text{cm}^2 \text{s}^{-1}$ )	$R$ (m)	$T$ (years)
LNGS	$(3.432 \pm 0.003) \cdot 10^{-8}$ [29]	10	29.41
SURF	$(5.31 \pm 0.17) \cdot 10^{-9}$ [30]	8	29.70
LSM	$(6.25 \pm 0.23) \cdot 10^{-9}$ [31]	6	44.86
SNOLAB	$(3.31 \pm 0.09) \cdot 10^{-10}$ [32]	9	232.93

1. Random sampling. A random point is generated inside a disk of radius  $R$  on the horizontal  $z = 0$  plane. We transport the direction vector to this point.
2. Rotation. We rotate the disk on  $z = 0$  until it becomes perpendicular to the direction vector.
3. Projection. The point on the rotated disk is projected to the external surface of the rock volume, assuming a linear trajectory.

The radius  $R$  of the sampling disk has to be large enough to cover the whole experimental setup, but at the same time not excessively large, as a very large disk could imply that we are sampling muons that have no physical meaning or that are so far away from the experiment that they are irrelevant for the simulation. Since the live-time of the simulation is estimated from the size of the disk, a large disk translates into more computational time needed to produce significant statistics. Since every muon has its initial position at the external surface of the shielding materials, the muon generator ensures that all the primary muons are propagated through at least 5 m of rock.

In Table 4 we summarised the experimentally measured muon fluxes at the locations of this work together with the radius of the sampling disk used in the muon generator and the equivalent live-time of the simulations.

## 3 Results

### 3.1 Muon-induced neutrons

Muons produce cascades of secondary particles when they interact with the different materials of the experiment. A full description of such cascades is complicated due to the types of particles and the diversity of physical processes involved. The interaction of cosmic muons with the shielding rock of the experiment is the main source of environmental neutrons. The rate of these neutrons, for the underground locations considered in this study, is about three orders of magnitude smaller compared to the neutrons produced in the spontaneous fission and  $(\alpha, n)$  reactions of  $^{238}\text{U}$  and  $^{232}\text{Th}$  present

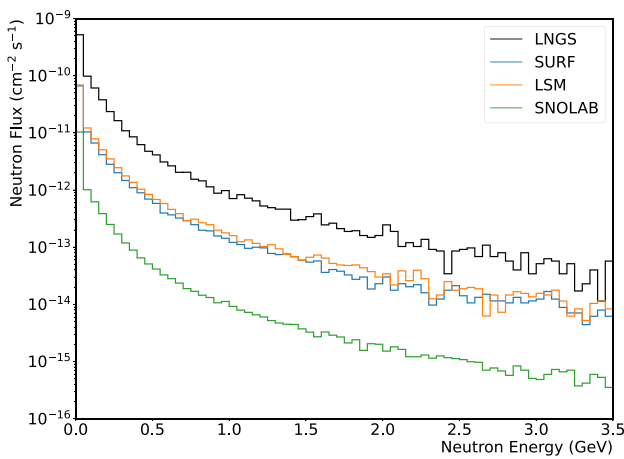


**Fig. 3** Spectrum of the muon-induced neutrons produced in rock (and concrete) for the underground laboratories considered in this work using the *Shielding* physics list. The energies of the histograms are the energies of the neutrons once they leave the rock and concrete walls and enter the experimental hall. The size of the energy bins is 50 MeV

in the rock and concrete. However, muon-induced neutrons can reach energies up to several GeV. It is thus very difficult to completely stop them and, therefore, they can be a potential background source inside the detector.

Figure 3 shows the energy spectrum of the muon-induced neutrons obtained in our simulations for the four underground laboratories using the *Shielding* physics list. The neutrons shown in the figure are the neutrons that enter the experimental hall from the rock and concrete walls. The double counting of the neutrons, such as neutrons bouncing off the walls, was avoided by a careful selection based on the track information provided by Geant4. For these, only the first step with the initial energy of the neutron entering the laboratory is considered.

### 3.2 Production of <sup>137</sup>Xe

For all the rates presented in this work, the value obtained by the *Shielding* physics list is the final production rate, and the systematic uncertainty is estimated using the other two:

$$\sigma_{sys}(R_{sh}) = \sqrt{\frac{(R_{sh} - R_{shL})^2 + (R_{sh} - R_{bic})^2}{2}} \quad (1)$$

where  $R_{sh}$ ,  $R_{shL}$ , and  $R_{bic}$  are the rates obtained with *Shielding*, *ShieldingLEND*, and *QGSP\_BIC\_HP* respectively.

For the total uncertainty in the rate, two extra components are considered: first, the uncertainty in the number of isotopes (statistical) and second the experimental uncertainty of the measured muon flux. The first is assumed to be Poisson-like distributed and therefore the associated uncertainty is  $\sqrt{n}$ , being  $n$  the number of produced isotopes. The uncertainty in

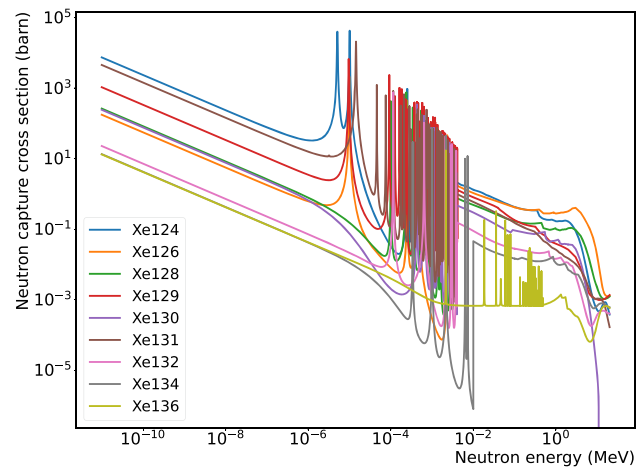


**Fig. 4** Neutron capture cross sections for the xenon isotopes as a function of the neutron energy, taken from [43]

the muon flux translates into an uncertainty in the simulated live-time ( $T$ ). Both components are then added in quadrature to provide the total uncertainty of the rate:

$$\sigma(R_{sh}) = R_{sh} \cdot \sqrt{\frac{1}{n} + \frac{\sigma^2(\phi)}{\phi^2}}, \quad (2)$$

where  $n$  is the number of isotopes and  $\phi$  the measured muon flux with uncertainty  $\sigma(\phi)$  as seen in Table 4.

Figure 4 shows the cross section for the neutron capture process in xenon isotopes as a function of the incident neutron energy.

Despite the neutron capture cross section being higher for low energy neutrons, there are resonances for energies below 1 MeV and therefore neutrons that are not fully thermal can be captured too. In addition, since <sup>136</sup>Xe has the smallest neutron capture cross section (olive curve), the amount of neutrons available to be captured by <sup>136</sup>Xe is reduced by the presence of the other xenon isotopes. Further studies are being performed to study the cosmogenic <sup>137</sup>Xe production rate as a function of the isotopic composition of xenon at several underground locations. This new study will give more information on whether using enriched-depleted xenon in DARWIN is more convenient for the scientific channels of interest.

Our simulations indicate that the muon-induced neutrons produced in the walls of the laboratory are properly thermalized and captured by the muon veto water tank and they do not contribute to the production of <sup>137</sup>Xe. We conclude that approximately 95% of the <sup>137</sup>Xe isotopes are produced by the capture of neutrons produced by muons crossing the liquid xenon. The rest are produced by secondary neutron cascades originated in the detector materials.

Table 5 summarizes the production of <sup>137</sup>Xe for the considered underground locations. In Appendix A the complete

**Table 5** Muon-induced  $^{137}\text{Xe}$  production rate at the different underground laboratories. The central value is the rate obtained with the `Shielding` physics list and the systematic error is calculated using the complementary simulations with the `ShieldingLEND` and `QGSP_BIC_HP` physics lists

Site	Rate ( $\text{kg}^{-1} \text{ year}^{-1}$ )
LNGS	$(8.22 \pm 0.27 \pm 1.00_{\text{sys}}) \cdot 10^{-4}$
SURF	$(1.42 \pm 0.12 \pm 0.21_{\text{sys}}) \cdot 10^{-4}$
LSM	$(1.65 \pm 0.11 \pm 0.30_{\text{sys}}) \cdot 10^{-4}$
SNOLAB	$(6.75 \pm 0.60 \pm 1.00_{\text{sys}}) \cdot 10^{-6}$

**Table 6** Muon-induced  $^3\text{H}$  production rate at the different underground laboratories. The central value is the rate obtained with the `Shielding` physics list and the systematic error is calculated using the complementary simulations with the `ShieldingLEND` and `QGSP_BIC_HP` physics lists

Site	Rate ( $\text{kg}^{-1} \text{ year}^{-1}$ )
LNGS	$(1.22 \pm 0.01 \pm 0.01_{\text{sys}}) \cdot 10^{-2}$
SURF	$(1.98 \pm 0.01 \pm 0.04_{\text{sys}}) \cdot 10^{-3}$
LSM	$(2.44 \pm 0.01 \pm 0.04_{\text{sys}}) \cdot 10^{-3}$
SNOLAB	$(1.40 \pm 0.05 \pm 0.50_{\text{sys}}) \cdot 10^{-4}$

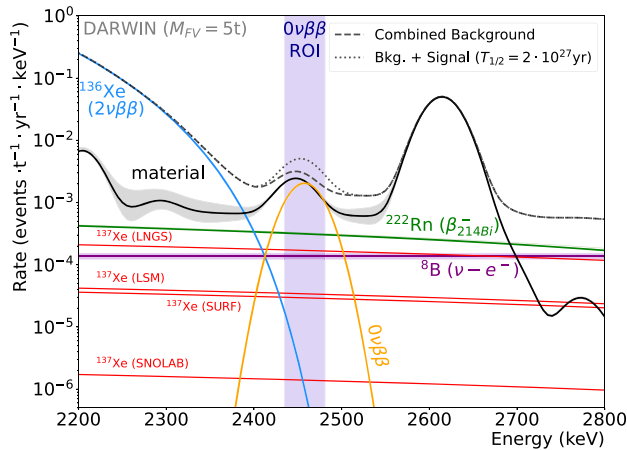


**Fig. 5** Expected background spectrum at the neutrinoless double beta decay ROI for a fiducial mass of 5 t [18, 44]. An hypothetical signal of 0.5 counts per year (corresponding to  $T_{1/2}^{0\nu} = 2 \cdot 10^{27}$  years) is shown for comparison. The red lines indicate the rates of  $^{137}\text{Xe}$  expected at the laboratories in this study, all below the expected  $^{222}\text{Rn}$  background

set of rates obtained for all locations with the three physics lists are shown. From those tables we have a maximum discrepancy of a factor  $\sim 20\%$  between rates, which is expected due to the different physical models used in the definitions of the lists.

The value obtained in this work for the  $^{137}\text{Xe}$  production rate at LNGS is a factor  $\sim 8$  smaller compared to previous DARWIN study of the sensitivity to the neutrinoless double beta decay [18]. In Fig. 5, the expected background spectrum around the neutrinoless double beta decay region of interest (ROI) is shown, assuming a fiducial mass of 5 t [44]. For reference, a signal rate of 0.5 counts per year is also displayed. The expected rates of  $^{137}\text{Xe}$  at the underground laboratories considered in this study are represented as red lines.

A more detailed description of the expected background index in the neutrinoless double beta decay ROI (2435 – 2481 keV) at LNGS is provided in Table 8 (see Appendix A).

With the results presented in this work, the contribution of the decay of  $^{137}\text{Xe}$  to the neutrinoless double beta decay

background is at the same level as the contribution of solar  $^8\text{B}$  neutrinos at all underground locations.

### 3.3 Production of tritium

In 2020, the XENON collaboration reported an excess of events at energies below 7 keV [15]. One of the possible explanations is the  $\beta$ -decay of tritium atoms present in the active xenon inside the TPC. This decay has a  $Q_\beta$  of 18.591 keV and a half-life of 12.3 years. It was reported that the excess would correspond to a tritium concentration of  $(6.2 \pm 2.0) \cdot 10^{-25} \text{ mol mol}^{-1}$ .

Tritium is mainly produced by neutron inelastic scattering and muon spallation processes. Although emanation from materials was considered as the primary source of tritium, cosmic muons and their secondary induced neutrons could be a continuous source of tritium. Spallation reactions of the xenon isotopes and in the surrounding materials of the TPC could induce the presence of tritium in the sensitive volume. Table 6 summarizes the production of  $^3\text{H}$  for the considered underground locations.

Assuming the worst case scenario, in which all the tritium that has been produced cannot be removed and it remains in the active volume, after one year at LNGS, we expect  $11.6^3\text{H ton}^{-1}$  or the equivalent of  $2.6 \cdot 10^{-27} \text{ mol mol}^{-1}$ . This value has a discrepancy of two orders of magnitude with the tritium concentration that could explain the XENON1T excess. In the analysis of low-energy electronic recoil data from the first science run of the XENONnT experiment, the excess observed in XENON1T disappeared [45].

In summary, cosmogenic production of tritium is not significant enough to make up all of the excess low-energy electronic recoil events.

### 3.4 Activation of other xenon isotopes

Neutron captures can produce xenon isotopes inside the TPC that are unstable. In the low-energy region (below 30 keV), the decays of these isotopes could be relevant for the WIMP and other rare-event searches. For example,  $^{125}\text{Xe}$  decays



**Table 7** Muon-induced  $^{125}\text{Xe}$ ,  $^{127}\text{Xe}$ ,  $^{133}\text{Xe}$  and  $^{135}\text{Xe}$  production rates (all processes) in  $\text{kg}^{-1} \text{y ears}^{-1}$  at the different underground laboratories. The central value is the rate obtained with the `Shielding` physics

list and the systematic error is calculated using the complementary simulations with the `ShieldingLEND` and `QGSP_BIC_HP` physics lists

Isotope	LNGS	SURF	LSM	SNOLAB
$^{125}\text{Xe}$	$(2.28 \pm 0.02 \pm 0.50_{\text{sys}}) \cdot 10^{-2}$	$(3.09 \pm 0.01 \pm 0.50_{\text{sys}}) \cdot 10^{-3}$	$(4.33 \pm 0.17 \pm 0.80_{\text{sys}}) \cdot 10^{-3}$	$(2.18 \pm 0.09 \pm 0.50_{\text{sys}}) \cdot 10^{-4}$
$^{127}\text{Xe}$	$(6.39 \pm 0.02 \pm 0.60_{\text{sys}}) \cdot 10^{-2}$	$(1.02 \pm 0.03 \pm 0.80_{\text{sys}}) \cdot 10^{-2}$	$(1.25 \pm 0.05 \pm 0.12_{\text{sys}}) \cdot 10^{-2}$	$(6.38 \pm 0.21 \pm 0.70_{\text{sys}}) \cdot 10^{-4}$
$^{133}\text{Xe}$	$(1.16 \pm 0.01 \pm 0.10_{\text{sys}}) \cdot 10^{-1}$	$(1.80 \pm 0.05 \pm 0.02_{\text{sys}}) \cdot 10^{-2}$	$(2.23 \pm 0.08 \pm 0.16_{\text{sys}}) \cdot 10^{-2}$	$(1.20 \pm 0.04 \pm 0.07_{\text{sys}}) \cdot 10^{-3}$
$^{135}\text{Xe}$	$(4.63 \pm 0.02 \pm 0.16_{\text{sys}}) \cdot 10^{-2}$	$(7.42 \pm 0.25 \pm 0.28_{\text{sys}}) \cdot 10^{-3}$	$(9.10 \pm 0.30 \pm 0.50_{\text{sys}}) \cdot 10^{-3}$	$(5.01 \pm 0.02 \pm 0.02_{\text{sys}}) \cdot 10^{-4}$

to  $^{125}\text{I}$  with a half-life of 16.9 h. The gamma lines from the  $^{125}\text{Xe}$  decay are above 200 keV, hence they are not of interest for the WIMP analysis. However, the  $^{125}\text{I}$  also decays to  $^{125}\text{Te}$ , with a half-life of 59.4 days. In this case, the three lines from the  $^{125}\text{I}$  decay are below 100 keV. They correspond to the atomic K-shell, L-shell, and M-shell with decreasing probability and produce peaks at 67.3, 40.4, and 36.5 keV, respectively. In addition to neutron capture, other processes such as muon spallation or photodisintegration contribute to the formation of the isotopes mentioned above.

The isotopes considered in this study are  $^{125}\text{Xe}$  ( $t_{1/2} = 16.9 \text{ h}$ ),  $^{127}\text{Xe}$  ( $t_{1/2} = 36.4 \text{ days}$ ),  $^{133}\text{Xe}$  ( $t_{1/2} = 5.24 \text{ days}$ ) and  $^{135}\text{Xe}$  ( $t_{1/2} = 9.14 \text{ h}$ ). The activation rates of these isotopes for the underground laboratories are shown in Table 7. We observe an agreement between the three physics lists used in our simulations. We can conclude that the production of these isotopes does not significantly impact the WIMP search analysis, but they would be relevant in other physics channels related to the ER energy range up to  $\mathcal{O}(100 \text{ keV})$ .

### 3.5 Activation of isotopes in the xenon storage system

Muon-induced neutrons coming from the walls of the laboratory are moderated in the water tank and they have no influence on the activation of isotopes such as  $^{137}\text{Xe}$ . However, the xenon storage and purification systems are placed outside the protection provided by the water tank, and exposed to high-energy neutrons and susceptible to activation. Since the liquid xenon is circulating between the purification systems and the TPC, radioactive isotopes activated outside the detector can end inside the active volume.

As the design of the DARWIN purification system is not finished yet, in a first approximation we simulated the storage system as a stainless-steel cylinder with a thickness of 0.5 cm, 0.5 m radius, and 5 m height at the LNGS Hall B, as seen in Fig. 6. In total, this column contains 11.2 tonnes of liquid xenon in addition to those already present inside the detector.

We simulated a total live-time of approximately 9.3 years using the information for muons provided by MUSUN in our muon generator and the `Shielding` physics list. From this simulation, we obtain production rates for tritium and  $^{137}\text{Xe}$  of  $10^{-2} \text{ kg}^{-1} \text{ year}^{-1}$  and  $3 \cdot 10^{-4} \text{ kg}^{-1} \text{ year}^{-1}$ , respectively.

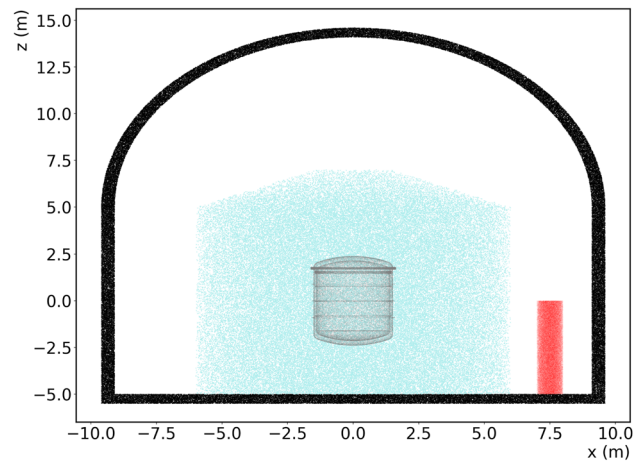


**Fig. 6** Cross-sectional view of the simulated LNGS experimental hall B with a storage column outside the water tank. The black region represents the concrete layer, the turquoise is the water tank, the grey is the cryostat and the red is the cylindrical storage column. The TPC and the shielding rock are removed for simplicity

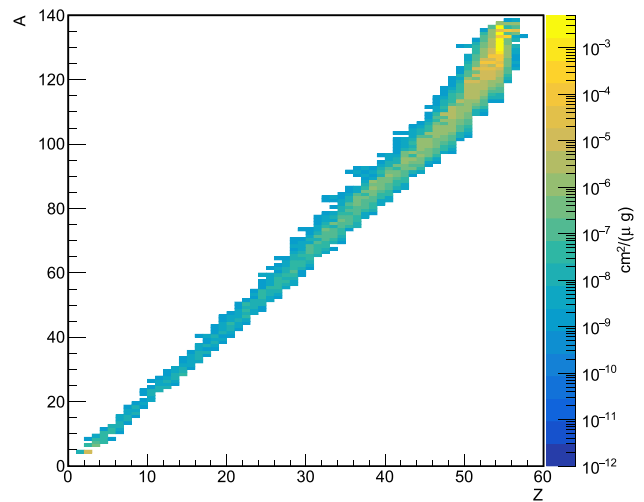


**Fig. 7** Muon-induced spallation yields (for  $A \geq 4$ ) simulated for LNGS using the `Shielding` physics list. The yields are expressed in  $\text{cm}^2/(\mu \cdot \text{g})$ . As in [46], we have used the LXe density ( $2.85 \text{ g cm}^{-3}$ ), the mean track length of the muons (171 cm), the livetime (29.41 years) and the rate of muons passing through the TPC ( $\approx 9 \mu \text{ h}^{-1}$ ) for the conversion of units

**Table 8** Expected background in the region of interest (ROI) for the neutrinoless double beta decay process (2435–2481 keV), assuming a fiducial mass of 5 t at LNGS, as published in [44]. These numbers correspond to the spectrum shown in Fig. 5. The first column indicates the type of background source, which is classified as external or intrinsic. The second column is the background index, given in  $\text{t}^{-1} \text{year}^{-1} \text{keV}^{-1}$ . The third column represents the expected rate in the ROI, in  $\text{year}^{-1}$ . The last column shows the relative statistical uncertainty of the rates

Type	Background index	Rate	Rel. uncertainty
External (5 t FV)			
$^{214}\text{Bi}$ peaks + continuum	$1.36 \cdot 10^{-3}$	0.313	$\pm 3.6\%$
$^{208}\text{Tl}$ continuum	$6.20 \cdot 10^{-4}$	0.143	$\pm 4.9\%$
$^{44}\text{Sc}$ continuum	$4.64 \cdot 10^{-6}$	0.001	$\pm 15.8\%$
Intrinsic contributions			
$^8\text{B}$ ( $\nu - e$ scattering)	$1.51 \cdot 10^{-4}$	0.035	$\pm 13.5\%$
$^{137}\text{Xe}$	$1.69 \cdot 10^{-4}$	0.039	$\pm 10.2\%$
$^{136}\text{Xe}$ ( $2\nu\beta\beta$ )	$5.78 \cdot 10^{-6}$	0.001	$\pm 17.0\%$
$^{222}\text{Rn}$ in LXe ( $0.1 \mu\text{Bq kg}^{-1}$ )	$3.09 \cdot 10^{-4}$	0.071	$\pm 1.6\%$
Total	$2.62 \cdot 10^{-3}$	0.603	$\pm 2.4\%$

These values are compatible with those shown in Tables 5 and 6. However, unshielded xenon is exposed to the radiation coming from the fission and ( $\alpha, n$ ) reactions from the rock and concrete walls, especially if it is placed near to them.

### 3.6 Muon-induced spallation products

The KamLAND-Zen collaboration recently published a list of isotopes produced after muon spallation that have a non-negligible impact on the ROI of the  $0\nu\beta\beta$  process [46]. In Table 9 (see Appendix A), we compare the rates of the isotopes that are produced in the Xe-LS of KamLAND-Zen (listed in Table IX of [46]) to those obtained from the simulations conducted for our detector placed at LNGS. For this comparison, we have scaled our rates using only the ratio between the muon fluxes at both locations to obtain an extrapolated value at Kamioka. It should be noted that the geometry, mean muon energy, and isotopic mixtures differ between both experiments, which may explain the discrepancies observed in some isotopes. Additionally, Fig. 7 shows the yields of the isotopes produced by muon spallation simulated at LNGS with the DARWIN geometry. The yields are given in  $\text{cm}^2/(\mu \text{g})$  using the conversion [46]:

$$R = \frac{N}{f_{\mu} \rho T L_{\mu}} \quad (3)$$

where  $f_{\mu}$  is the rate of muons crossing the TPC ( $\approx 9 \mu \text{h}^{-1}$ ),  $\rho$  the LXe density ( $2.85 \text{g cm}^{-3}$ ),  $T$  the simulated livetime (29.41 years) and  $L_{\mu}$  the mean track length (171 cm). In the figure, only isotopes with  $A \geq 4$  are displayed.

This figure can be compared to the simulations done by KamLAND-Zen for natural xenon (Fig. 12 of [46]). Although both figures seem to exhibit similar behavior, factors such as the choice of the physics list can have a significant influence on the values of the presented rates. More detailed simulations are ongoing, and more precise conclusions will be presented in future works.

## 4 Summary and conclusions

We have performed Monte Carlo simulations of the cosmogenic background for the DARWIN experiment. The study was done for four underground laboratories that are candidates for the location of the detector.

We developed a custom-made DARWIN-Geant4 simulation framework in which we implemented new features to perform full muon simulations. First, we performed a detailed simulation of the underground experimental halls. Second, a muon generator that samples primaries using the realistic energy-angle correlation provided by the MUSIC-MUSUN software packages was developed.

We presented an estimate of the cosmogenic activation rates due to muon-induced neutrons in rock and concrete,  $^{137}\text{Xe}$  and tritium. These isotopes are known to have non-negligible contributions to the background of physics channels such as the neutrinoless double beta decay and low-energy electronic recoils. In this work, we report a  $^{137}\text{Xe}$  production rate  $\sim 8$  times smaller than previous results for DARWIN [18]. This updated value places the  $^{137}\text{Xe}$  contribution to the background of neutrinoless double beta decay in  $^{136}\text{Xe}$  at a level below the scattering of  $^8\text{B}$  neutrinos with electrons at all underground locations, thereby making all of these locations suitable for the search for this process. Therefore, additional selection criteria have to be taken into account in the decision process leading to the final location of the DARWIN experiment. In addition, other xenon isotopes can be activated due to spallation processes, neutron captures from the muon secondary cascades or other inelastic processes. These can also contribute to the background at low energies, relevant for the WIMP search. More detailed studies are in progress to assess their influence on the sensitivity of DARWIN to various physics channels.

**Acknowledgements** This work was supported by the Swiss National Science Foundation under Grants no 200020-162501 and no 200020-175863, by the European Union's Horizon 2020 research and innovation programme under the Marie Skłodowska-Curie Grant agreements no 674896, no 690575 and no 691164, by the European Research Council (ERC) Grant agreements no 742789 (Xenoscope) and no 724320 (ULTIMATE), by the Max-Planck-Gesellschaft, by the Deutsche Forschungsgemeinschaft (DFG) under GRK-2149, by the US National Science Foundation (NSF) Grants no 1719271 and no 1940209, by the Portuguese FCT, by the Dutch Science Council (NWO), by the Ministry of Education, Science and Technological Development of the Republic

of Serbia and by Grant ST/N000838/1 from Science and Technology Facilities Council (UK). The authors would like to also thank Prof. V. Kudryavtsev for letting us use the MUSUN software.

**Data Availability Statement** This manuscript has no associated data or the data will not be deposited. [Authors’ comment: This study is based on simulations of a detector that is in the design phase, so there is no experimental data associated with it.]

**Open Access** This article is licensed under a Creative Commons Attribution 4.0 International License, which permits use, sharing, adaptation, distribution and reproduction in any medium or format, as long as you give appropriate credit to the original author(s) and the source, provide a link to the Creative Commons licence, and indicate if changes were made. The images or other third party material in this article are included in the article’s Creative Commons licence, unless indicated otherwise in a credit line to the material. If material is not included in the article’s Creative Commons licence and your intended use is not permitted by statutory regulation or exceeds the permitted use, you will need to obtain permission directly from the copyright holder. To view a copy of this licence, visit <http://creativecommons.org/licenses/by/4.0/>. Funded by SCOAP<sup>3</sup>.

### Appendix A: Detailed tables of the production rates

In this work we have performed simulations with three different physics lists distributed with Geant4: `Shielding`, `ShieldingLEND`, and `QGSP_BIC_HP`. Each list is constructed using hadronic and electromagnetic models together with a set of cross section databases. It is therefore possible to observe differences in the relative rates of processes such as neutron yields or isotope activation, reason why such differences have been propagated as uncertainties in these results.

For reference, Fig. 8 shows a comparative table of the lists used in this work. For each list, the hadronic component

consists of elastic, inelastic and capture-stopping models, depending on the energy of the particle. The name convention used on the table for the models is: Quark-gluon String with Precompound (QGSP), Fritiof Parton model with Precompound (FTFP), Binary Light Ion Cascade (BIC), CHiral Invariant Phase Space (CHIPS), Low Energy Nuclear Data (LEND), High Precision neutron model (HP) (Tables 10, 11, 12).

Shielding	Elastic model	NeutronHP	CHIPS	
	Inelastic model	NeutronHP	Bertini	FTFP
	Capture model	NeutronHP	nRadCapture	
ShieldingLEND	Elastic model	LEND	CHIPS	
	Inelastic model	LEND	Bertini	FTFP
	Capture model	LEND	nRadCapture	
QGSP_BIC_HP	Elastic model	NeutronHP	CHIPS	
	Inelastic model	NeutronHP	BIC	QGSP
	Capture model	NeutronHP	nRadCapture	

1 keV
1 MeV
1 GeV
1 TeV

**Fig. 8** Hadronic models defined in the Geant4 physics lists considered in this study. The energy scale at the bottom is placed for visual reference. The detailed energy ranges for each model is found in the Geant4 physics list guide [41]. Cross sections libraries used for each model are not shown

**Table 9** Simulated production rates (in  $\text{kg}^{-1} \text{ year}^{-1}$ , kilograms of natural xenon and year) of dominant isotopes resulting from muon-spallation processes using the `Shielding` physics list at the LNGS underground laboratory. These isotopes have been extracted from Table IX in reference [46] and have a potential non-negligible impact on the region of interest (ROI) of the  $0\nu\beta\beta$  process. The fifth column represents their expected rates in the ROI (2435–2481 keV). These rates have been estimated, for each isotope, by taking the ratio between the total rate and

the rate in the ROI provided in [46], and then linearly scaled to approximate the rate in the ROI of DARWIN. The rates have been extrapolated to the Kamioka underground laboratory using only the ratio between their muon fluxes ( $\phi_{\mu, \text{Kamioka}}/\phi_{\mu, \text{LNGS}} = 4.6037$ ). The last column displays the simulated rates reported in [46], converted to  $\text{kg}^{-1} \text{ year}^{-1}$  (kilograms of enriched xenon and year). For this conversion, we utilized the 24 t of the Xe-LS, which contains 745 kg of enriched xenon

Isotope	$\tau_{1/2}$ (s)	$Q$ (MeV)	Rate (LNGS)	ROI (LNGS)	Rate (Kamioka)	Xe-LS (KamLAND-Zen)
<sup>88</sup> Y	$9.212 \cdot 10^6$	3.62 (EC/ $\beta^+\gamma$ )	$2.61 \cdot 10^{-4}$	$3.43 \cdot 10^{-5}$	$1.20 \cdot 10^{-3}$	$1.60 \cdot 10^{-3}$
<sup>90m1</sup> Zr	$8.092 \cdot 10^{-1}$	2.31 (IT)	$1.80 \cdot 10^{-4}$	$3.05 \cdot 10^{-6}$	$8.29 \cdot 10^{-4}$	$1.09 \cdot 10^{-3}$
<sup>90</sup> Nb	$5.256 \cdot 10^4$	6.11 (EC/ $\beta^+\gamma$ )	$1.77 \cdot 10^{-4}$	$5.87 \cdot 10^{-6}$	$8.14 \cdot 10^{-4}$	$1.11 \cdot 10^{-3}$
<sup>96</sup> Tc	$3.698 \cdot 10^5$	2.97 (EC/ $\beta^+\gamma$ )	$7.19 \cdot 10^{-5}$	$1.92 \cdot 10^{-6}$	$3.31 \cdot 10^{-4}$	$6.94 \cdot 10^{-4}$
<sup>98</sup> Rh	$5.232 \cdot 10^2$	5.06 (EC/ $\beta^+\gamma$ )	$3.13 \cdot 10^{-4}$	$6.00 \cdot 10^{-6}$	$1.44 \cdot 10^{-3}$	$8.94 \cdot 10^{-4}$
<sup>100</sup> Rh	$7.488 \cdot 10^4$	3.63 (EC/ $\beta^+\gamma$ )	$5.66 \cdot 10^{-4}$	$2.79 \cdot 10^{-5}$	$2.61 \cdot 10^{-3}$	$2.75 \cdot 10^{-3}$
<sup>104</sup> Ag	$4.152 \cdot 10^3$	4.28 (EC/ $\beta^+\gamma$ )	$1.73 \cdot 10^{-4}$	$1.70 \cdot 10^{-6}$	$7.96 \cdot 10^{-4}$	$1.88 \cdot 10^{-3}$
<sup>104m1</sup> Ag	$2.010 \cdot 10^3$	4.28 (EC/ $\beta^+\gamma$ )	$3.89 \cdot 10^{-4}$	$8.29 \cdot 10^{-6}$	$1.79 \cdot 10^{-3}$	$1.30 \cdot 10^{-3}$
<sup>107</sup> In	$1.944 \cdot 10^3$	3.43 (EC/ $\beta^+\gamma$ )	$3.00 \cdot 10^{-4}$	$5.60 \cdot 10^{-6}$	$1.38 \cdot 10^{-3}$	$1.57 \cdot 10^{-3}$

**Table 9** continued

Isotope	$\tau_{1/2}$ (s)	$Q$ (MeV)	Rate (LNGS)	ROI (LNGS)	Rate (Kamioka)	Xe-LS (KamLAND-Zen)
$^{108}\text{In}$	$3.480 \cdot 10^3$	5.16 (EC/ $\beta^+\gamma$ )	$2.65 \cdot 10^{-4}$	$1.60 \cdot 10^{-5}$	$1.22 \cdot 10^{-3}$	$2.28 \cdot 10^{-3}$
$^{110}\text{In}$	$1.771 \cdot 10^4$	3.89 (EC/ $\beta^+\gamma$ )	$2.48 \cdot 10^{-4}$	$7.32 \cdot 10^{-6}$	$1.14 \cdot 10^{-3}$	$2.77 \cdot 10^{-3}$
$^{110m1}\text{In}$	$4.146 \cdot 10^3$	3.89 (EC/ $\beta^+\gamma$ )	$9.02 \cdot 10^{-4}$	$2.23 \cdot 10^{-5}$	$4.15 \cdot 10^{-3}$	$4.13 \cdot 10^{-3}$
$^{109}\text{Sn}$	$1.080 \cdot 10^3$	3.85 (EC/ $\beta^+\gamma$ )	$4.68 \cdot 10^{-4}$	$1.37 \cdot 10^{-5}$	$2.15 \cdot 10^{-3}$	$2.77 \cdot 10^{-3}$
$^{113}\text{Sb}$	$4.002 \cdot 10^2$	3.92 (EC/ $\beta^+\gamma$ )	$5.13 \cdot 10^{-4}$	$1.05 \cdot 10^{-5}$	$2.36 \cdot 10^{-3}$	$2.72 \cdot 10^{-3}$
$^{114}\text{Sb}$	$2.094 \cdot 10^2$	5.88 (EC/ $\beta^+\gamma$ )	$9.44 \cdot 10^{-4}$	$8.36 \cdot 10^{-6}$	$4.34 \cdot 10^{-3}$	$3.49 \cdot 10^{-3}$
$^{115}\text{Sb}$	$1.926 \cdot 10^3$	3.03 (EC/ $\beta^+\gamma$ )	$1.14 \cdot 10^{-3}$	$5.53 \cdot 10^{-6}$	$5.25 \cdot 10^{-3}$	$9.87 \cdot 10^{-3}$
$^{116}\text{Sb}$	$9.480 \cdot 10^2$	4.71 (EC/ $\beta^+\gamma$ )	$2.15 \cdot 10^{-3}$	$2.14 \cdot 10^{-5}$	$9.90 \cdot 10^{-3}$	$1.10 \cdot 10^{-2}$
$^{118}\text{Sb}$	$2.160 \cdot 10^2$	3.66 (EC/ $\beta^+\gamma$ )	$3.88 \cdot 10^{-3}$	$6.53 \cdot 10^{-5}$	$1.79 \cdot 10^{-2}$	$1.51 \cdot 10^{-2}$
$^{124}\text{Sb}$	$5.201 \cdot 10^6$	2.90 (EC/ $\beta^-\gamma$ )	$2.71 \cdot 10^{-4}$	$1.06 \cdot 10^{-5}$	$1.25 \cdot 10^{-3}$	$6.35 \cdot 10^{-4}$
$^{115}\text{Te}$	$3.480 \cdot 10^2$	4.64 (EC/ $\beta^+\gamma$ )	$8.14 \cdot 10^{-4}$	$1.04 \cdot 10^{-5}$	$3.75 \cdot 10^{-3}$	$1.46 \cdot 10^{-3}$
$^{117}\text{Te}$	$3.720 \cdot 10^3$	3.54 (EC/ $\beta^+\gamma$ )	$1.71 \cdot 10^{-3}$	$1.97 \cdot 10^{-5}$	$7.87 \cdot 10^{-3}$	$6.98 \cdot 10^{-3}$
$^{119}\text{I}$	$1.146 \cdot 10^3$	3.51 (EC/ $\beta^+\gamma$ )	$1.93 \cdot 10^{-3}$	$2.52 \cdot 10^{-5}$	$8.90 \cdot 10^{-3}$	$6.27 \cdot 10^{-3}$
$^{120}\text{I}$	$4.896 \cdot 10^3$	5.62 (EC/ $\beta^+\gamma$ )	$3.29 \cdot 10^{-3}$	$4.13 \cdot 10^{-5}$	$1.51 \cdot 10^{-2}$	$1.12 \cdot 10^{-2}$
$^{122}\text{I}$	$2.178 \cdot 10^2$	4.23 (EC/ $\beta^+\gamma$ )	$8.48 \cdot 10^{-3}$	$1.28 \cdot 10^{-4}$	$3.90 \cdot 10^{-2}$	$2.31 \cdot 10^{-2}$
$^{124}\text{I}$	$3.608 \cdot 10^5$	3.16 (EC/ $\beta^+\gamma$ )	$4.65 \cdot 10^{-3}$	$7.00 \cdot 10^{-5}$	$2.14 \cdot 10^{-2}$	$1.94 \cdot 10^{-2}$
$^{130}\text{I}$	$4.450 \cdot 10^4$	2.95 ( $\beta^-\gamma$ )	$4.55 \cdot 10^{-3}$	$1.38 \cdot 10^{-4}$	$2.10 \cdot 10^{-2}$	$1.40 \cdot 10^{-2}$
$^{132}\text{I}$	$8.262 \cdot 10^3$	3.58 ( $\beta^-\gamma$ )	$2.11 \cdot 10^{-3}$	$9.60 \cdot 10^{-5}$	$9.71 \cdot 10^{-3}$	$5.02 \cdot 10^{-3}$
$^{134}\text{I}$	$3.150 \cdot 10^3$	4.18 ( $\beta^-\gamma$ )	$8.14 \cdot 10^{-4}$	$2.50 \cdot 10^{-5}$	$3.75 \cdot 10^{-3}$	$2.15 \cdot 10^{-3}$
$^{121}\text{Xe}$	$2.406 \cdot 10^3$	3.75 (EC/ $\beta^+\gamma$ )	$2.26 \cdot 10^{-3}$	$5.60 \cdot 10^{-5}$	$1.04 \cdot 10^{-2}$	$6.35 \cdot 10^{-3}$
$^{125}\text{Cs}$	$2.406 \cdot 10^3$	3.09 (EC/ $\beta^+\gamma$ )	$5.72 \cdot 10^{-4}$	$3.40 \cdot 10^{-6}$	$2.63 \cdot 10^{-3}$	$3.13 \cdot 10^{-3}$
$^{126}\text{Cs}$	$9.840 \cdot 10^1$	4.82 (EC/ $\beta^+\gamma$ )	$5.92 \cdot 10^{-4}$	$1.07 \cdot 10^{-5}$	$2.73 \cdot 10^{-3}$	$9.41 \cdot 10^{-4}$
$^{128}\text{Cs}$	$2.196 \cdot 10^2$	3.93 (EC/ $\beta^+\gamma$ )	$8.79 \cdot 10^{-4}$	$1.56 \cdot 10^{-5}$	$4.10 \cdot 10^{-3}$	$2.69 \cdot 10^{-3}$

**Table 10** Muon-induced  $^{137}\text{Xe}$  production rate at the different underground laboratories given in  $\text{kg}^{-1}\text{year}^{-1}$ . We compare the results obtained with the Shielding, ShieldingLEND and QGSP\_BIC\_HP physics lists

Site	Shielding	ShieldingLEND	QGSP_BIC_HP
LNGS	$8.22 \cdot 10^{-4}$	$8.46 \cdot 10^{-4}$	$6.87 \cdot 10^{-4}$
SURF	$1.42 \cdot 10^{-4}$	$1.35 \cdot 10^{-4}$	$1.13 \cdot 10^{-4}$
LSM	$1.65 \cdot 10^{-4}$	$1.66 \cdot 10^{-4}$	$1.23 \cdot 10^{-4}$
SNOLAB	$6.75 \cdot 10^{-6}$	$8.10 \cdot 10^{-6}$	$6.75 \cdot 10^{-6}$

**Table 11** Muon-induced  $^3\text{H}$  production rate at the different underground laboratories given in  $\text{kg}^{-1}\text{year}^{-1}$ . We compare the results obtained with the Shielding, ShieldingLEND and QGSP\_BIC\_HP physics lists

Site	Shielding	ShieldingLEND	QGSP_BIC_HP
LNGS	$1.16 \cdot 10^{-2}$	$1.17 \cdot 10^{-2}$	$1.33 \cdot 10^{-2}$
SURF	$1.82 \cdot 10^{-3}$	$1.68 \cdot 10^{-3}$	$2.45 \cdot 10^{-3}$
LSM	$2.17 \cdot 10^{-3}$	$2.35 \cdot 10^{-3}$	$2.79 \cdot 10^{-3}$
SNOLAB	$1.05 \cdot 10^{-4}$	$1.63 \cdot 10^{-4}$	$1.51 \cdot 10^{-4}$

**Table 12** Muon-induced activation rates (all processes) of  $^{125}\text{Xe}$ ,  $^{127}\text{Xe}$ ,  $^{133}\text{Xe}$  and  $^{135}\text{Xe}$  given in  $\text{kg}^{-1}\text{year}^{-1}$ . We compare the results obtained with the Shielding, ShieldingLEND and QGSP\_BIC\_HP physics lists

List	Isotope	LNGS	SURF	LSM	SNOLAB
Shielding	$^{125}\text{Xe}$	$2.28 \cdot 10^{-2}$	$3.29 \cdot 10^{-3}$	$4.33 \cdot 10^{-3}$	$2.18 \cdot 10^{-4}$
ShieldingLEND		$2.41 \cdot 10^{-2}$	$3.36 \cdot 10^{-3}$	$4.94 \cdot 10^{-3}$	$2.59 \cdot 10^{-4}$
QGSP_BIC_HP		$1.62 \cdot 10^{-2}$	$2.62 \cdot 10^{-3}$	$3.33 \cdot 10^{-3}$	$1.63 \cdot 10^{-4}$
Shielding	$^{127}\text{Xe}$	$6.39 \cdot 10^{-2}$	$1.02 \cdot 10^{-2}$	$1.25 \cdot 10^{-2}$	$6.38 \cdot 10^{-4}$
ShieldingLEND		$6.78 \cdot 10^{-2}$	$1.11 \cdot 10^{-2}$	$1.40 \cdot 10^{-2}$	$7.24 \cdot 10^{-4}$
QGSP_BIC_HP		$5.59 \cdot 10^{-2}$	$9.52 \cdot 10^{-3}$	$1.18 \cdot 10^{-2}$	$6.01 \cdot 10^{-4}$
Shielding	$^{133}\text{Xe}$	$1.16 \cdot 10^{-1}$	$1.80 \cdot 10^{-2}$	$2.23 \cdot 10^{-2}$	$1.20 \cdot 10^{-3}$



Table 12 continued

List	Isotope	LNGS	SURF	LSM	SNOLAB
ShieldingLEND		$1.20 \cdot 10^{-1}$	$1.82 \cdot 10^{-2}$	$2.45 \cdot 10^{-2}$	$1.29 \cdot 10^{-3}$
QGSP_BIC_HP		$1.10 \cdot 10^{-1}$	$1.81 \cdot 10^{-2}$	$2.24 \cdot 10^{-2}$	$1.18 \cdot 10^{-3}$
Shielding	$^{135}\text{Xe}$	$4.63 \cdot 10^{-2}$	$7.42 \cdot 10^{-3}$	$9.10 \cdot 10^{-3}$	$5.01 \cdot 10^{-4}$
ShieldingLEND		$4.80 \cdot 10^{-2}$	$7.42 \cdot 10^{-3}$	$9.70 \cdot 10^{-3}$	$5.15 \cdot 10^{-4}$
QGSP_BIC_HP		$4.47 \cdot 10^{-2}$	$7.82 \cdot 10^{-3}$	$9.34 \cdot 10^{-3}$	$5.17 \cdot 10^{-4}$

## References

- XENON Collaboration, E. Aprile et al., Dark matter search results from a one ton-year exposure of XENON1T. *Phys. Rev. Lett.* **121**, 111302 (2018). <https://doi.org/10.1103/PhysRevLett.121.111302>. [arXiv:1805.12562](https://arxiv.org/abs/1805.12562)
- LUX Collaboration, D.S. Akerib et al., Results from a search for dark matter in the complete LUX exposure. *Phys. Rev. Lett.* **118**, 021303 (2017). <https://doi.org/10.1103/PhysRevLett.118.021303>. [arXiv:1608.07648](https://arxiv.org/abs/1608.07648)
- XENON Collaboration, E. Aprile et al., First dark matter search with nuclear recoils from the XENONnT experiment. *Phys. Rev. Lett.* **131**, 041003 (2023). <https://doi.org/10.1103/PhysRevLett.131.041003>
- LUX- ZEPLIN Collaboration, J. Aalbers et al., First dark matter search results from the LUX-ZEPLIN (LZ) experiment. *Phys. Rev. Lett.* **131**, 041002 (2023). <https://doi.org/10.1103/PhysRevLett.131.041002>
- PANDAX- 4T Collaboration, Y. Meng et al., Dark matter search results from the PandaX-4T commissioning run. *Phys. Rev. Lett.* **127**, 261802 (2021). <https://doi.org/10.1103/PhysRevLett.127.261802>. [arXiv:2107.13438](https://arxiv.org/abs/2107.13438)
- EXO- 200 Collaboration, G. Anton et al., Search for neutrinoless double- $\beta$  decay with the complete EXO-200 dataset. *Phys. Rev. Lett.* **123**, 161802 (2019). <https://doi.org/10.1103/PhysRevLett.123.161802>. [arXiv:1906.02723](https://arxiv.org/abs/1906.02723)
- KAMLAND- ZEN Collaboration, A. Gando et al., Search for Majorana Neutrinos near the Inverted Mass Hierarchy Region with KamLAND-Zen. *Phys. Rev. Lett.* **117**, 082503 (2016). <https://doi.org/10.1103/PhysRevLett.117.082503>. [arXiv:1605.02889](https://arxiv.org/abs/1605.02889)
- NEXT Collaboration, P. Ferrario et al., First proof of topological signature in the high pressure xenon gas TPC with electroluminescence amplification for the NEXT experiment. *JHEP* **01**, 104 (2016). [https://doi.org/10.1007/JHEP01\(2016\)104](https://doi.org/10.1007/JHEP01(2016)104). [arXiv:1507.05902](https://arxiv.org/abs/1507.05902)
- NEXO Collaboration, J.B. Albert et al., Sensitivity and discovery potential of nEXO to neutrinoless double beta decay. *Phys. Rev. C* **97**, 065503 (2018). <https://doi.org/10.1103/PhysRevC.97.065503>. [arXiv:1710.05075](https://arxiv.org/abs/1710.05075)
- KAMLAND- ZEN Collaboration, Y. Gando et al., The nylon balloon for xenon loaded liquid scintillator in KamLAND-Zen 800 neutrinoless double-beta decay search experiment. *Joi* **16**, P08023 (2021). <https://doi.org/10.1088/1748-0221/16/08/P08023>
- J.J. Gomez-Cadenas, Status and prospects of the NEXT experiment for neutrinoless double beta decay searches. in: 54th Rencontres de Moriond on Electroweak Interactions and Unified Theories (2019), pp. 201–206. [arxiv:1906.01743](https://arxiv.org/abs/1906.01743)
- XENON Collaboration, E. Aprile et al., Observation of two-neutrino double electron capture in  $^{124}\text{Xe}$  with XENON1T. *Nature* **568**, 532–535 (2019). <https://doi.org/10.1038/s41586-019-1124-4>. [arXiv:1904.11002](https://arxiv.org/abs/1904.11002)
- XENON Collaboration, E. Aprile et al., Search for coherent elastic scattering of solar  $^8\text{B}$  neutrinos in the XENON1T dark matter experiment. *Phys. Rev. Lett.* **126**, 091301 (2021). <https://doi.org/10.1103/PhysRevLett.126.091301>. [arXiv:2012.02846](https://arxiv.org/abs/2012.02846)
- LUX Collaboration, D.S. Akerib et al., First searches for axions and axionlike particles with the LUX experiment. *Phys. Rev. Lett.* **118**, 261301 (2017). <https://doi.org/10.1103/PhysRevLett.118.261301>. [arXiv:1704.02297](https://arxiv.org/abs/1704.02297)
- XENON Collaboration, E. Aprile et al., Excess electronic recoil events in XENON1T. *Phys. Rev. D* **102**, 072004 (2020). <https://doi.org/10.1103/PhysRevD.102.072004>. [arXiv:2006.09721](https://arxiv.org/abs/2006.09721)
- DARWIN Collaboration, J. Aalbers et al., DARWIN: towards the ultimate dark matter detector. *JCAP* **11**, 017 (2016). <https://doi.org/10.1088/1475-7516/2016/11/017>. [arXiv:1606.07001](https://arxiv.org/abs/1606.07001)
- DARWIN Collaboration, J. Aalbers et al., Solar neutrino detection sensitivity in DARWIN via electron scattering. *Eur. Phys. J. C* **80**, 1133 (2020). <https://doi.org/10.1140/epjc/s10052-020-08602-7>. [arXiv:2006.03114](https://arxiv.org/abs/2006.03114)
- DARWIN Collaboration, F. Agostini et al., Sensitivity of the DARWIN observatory to the neutrinoless double beta decay of  $^{136}\text{Xe}$ . *Eur. Phys. J. C* **80**, 808 (2020). <https://doi.org/10.1140/epjc/s10052-020-8196-z>. [arXiv:2003.13407](https://arxiv.org/abs/2003.13407)
- L. Baudis, A. Kish, F. Piastra, M. Schumann, Cosmogenic activation of xenon and copper. *Eur. Phys. J. C* **75**, 485 (2015). <https://doi.org/10.1140/epjc/s10052-015-3711-3>. [arXiv:1507.03792](https://arxiv.org/abs/1507.03792)
- NEXT Collaboration, L. Rogers et al., Mitigation of backgrounds from cosmogenic  $^{137}\text{Xe}$  in xenon gas experiments using  $^3\text{He}$  neutron capture. *J. Phys. G Nucl. Part. Phys.* **47**, (2020). <https://doi.org/10.1088/1361-6471/ab8915>. [arXiv:2001.11147](https://arxiv.org/abs/2001.11147)
- KAMLAND- ZEN Collaboration, S. Abe et al., Search for the Majorana nature of neutrinos in the inverted mass ordering region with KamLAND-Zen. *Phys. Rev. Lett.* **130**, 051801 (2023). <https://doi.org/10.1103/PhysRevLett.130.051801>. [arXiv:2203.02139](https://arxiv.org/abs/2203.02139)
- S. Agostinelli et al., Geant4, a simulation toolkit. *NIM A* **506**, 250–303 (2003). [https://doi.org/10.1016/S0168-9002\(03\)01368-8](https://doi.org/10.1016/S0168-9002(03)01368-8)
- E.-I. Esch, T. Bowles, A. Hime, A. Pichlmaier, R. Reifarh, H. Wollnik, The cosmic ray muon flux at WIPP. *NIM A* **538**, 516–525 (2005). <https://doi.org/10.1016/j.nima.2004.09.005>
- W. Trzaska, M. Slupecki, I. Bandac et al., Cosmic-ray muon flux at Canfranc Underground Laboratory. *Eur. Phys. J. C* **79**, 721 (2019). <https://doi.org/10.1140/epjc/s10052-019-7239-9>. [arXiv:1902.00868](https://arxiv.org/abs/1902.00868)
- C. Zhang, D.-M. Mei, Measuring muon-induced neutrons with liquid scintillation detector at Soudan mine. *Phys. Rev. D* **90**, 122003 (2014). <https://doi.org/10.1103/PhysRevD.90.122003>
- Y. Zhang et al., First measurement of radioactive isotope production through cosmic-ray muon spallation in Super-Kamiokande IV. *Phys. Rev. D* **93**, 012004 (2016). <https://doi.org/10.1103/PhysRevD.93.012004>
- M. Robinson, V. Kudryavtsev, R. Lüscher, J. McMillan, P. Lightfoot, N. Spooner et al., Measurements of muon flux at 1070 m vertical depth in the Boulby Underground Laboratory. *NIM A* **511**, 347–353 (2003). [https://doi.org/10.1016/S0168-9002\(03\)01973-9](https://doi.org/10.1016/S0168-9002(03)01973-9)
- W.D. Melbourne, SABRE South at the Stawell Underground Physics Laboratory. *J. Phys. Conf. Ser.* **2156**, 012064 (2021). <https://doi.org/10.1088/1742-6596/2156/1/012064>

29. M. Agostini et al., Modulations of the cosmic muon signal in ten years of Borexino data. *JCAP* **2019**, 046 (2019). <https://doi.org/10.1088/1475-7516/2019/02/046>. [arXiv:1808.04207](https://arxiv.org/abs/1808.04207)
30. N. Abgrall et al., Muon flux measurements at the Davis campus of the Sanford underground research facility with the Majorana demonstrator veto system. *Astropart. Phys.* **93**, 70–75 (2017). <https://doi.org/10.1016/j.astropartphys.2017.01.013>. [arXiv:1602.07742](https://arxiv.org/abs/1602.07742)
31. B. Schmidt et al., Muon-induced background in the EDELWEISS dark matter search. *Astropart. Phys.* **44**, 28–39 (2013). <https://doi.org/10.1016/j.astropartphys.2013.01.014>. [arXiv:1302.7112](https://arxiv.org/abs/1302.7112)
32. SNO Collaboration, B. Aharmim et al., Measurement of the cosmic ray and neutrino-induced muon flux at the Sudbury neutrino observatory. *Phys. Rev. D* **80**, 012001 (2009). <https://doi.org/10.1103/PhysRevD.80.012001>. [arXiv:0902.2776](https://arxiv.org/abs/0902.2776)
33. JNE Collaboration, Z. Guo et al., Muon flux measurement at China Jinping Underground Laboratory. *Chin. Phys. C* **45**, 025001(2021). <https://doi.org/10.1088/1674-1137/abccae>. [arXiv:2007.15925](https://arxiv.org/abs/2007.15925)
34. M. Selvi, Study of the performances of the shield and muon veto of the XENON1T experiment. *PoS IDM2010*, 053 (2011). <https://doi.org/10.22323/1.110.0053>
35. H. Wulandari, J. Jochum, W. Rau, F. von Feilitzsch, Neutron flux at the Gran Sasso underground laboratory revisited. *Astropart. Phys.* **22**, 313–322 (2004). <https://doi.org/10.1016/j.astropartphys.2004.07.005>
36. D.M. Mei, C. Zhang, K. Thomas, F. Gray, Early results on radioactive background characterization for Sanford Laboratory and DUSEL experiments. *Astropart. Phys.* **34**, 33–39 (2010). <https://doi.org/10.1016/j.astropartphys.2010.04.003>. [arXiv:0912.0211](https://arxiv.org/abs/0912.0211)
37. H. Kluck, *Measurement of the Cosmic-Induced Neutron Yield at the Modane Underground Laboratory* (Springer, Berlin, 2015). <https://doi.org/10.1007/978-3-319-18527-9>
38. SNOLAB. Snolab user's handbook revision 2. (2006)
39. L. Baudis, A. Behrens, A. Ferella, A. Kish, T.M. Undagoitia, D. Mayani et al., Performance of the Hamamatsu R11410 photomultiplier tube in cryogenic xenon environments. *JINST* **8**, P04026 (2013). <https://doi.org/10.1088/1748-0221/8/04/p04026>. [arXiv:1303.0226](https://arxiv.org/abs/1303.0226)
40. DIN 28011: Gewölbte Böden-Klöpferform. Deutsches Institut für Normung e.V. (DIN). (2012). <https://www.din.de/de/mitwirken/normenausschuesse/fnca/veroeffentlichungen/wdc-beuth:din21:151854193>
41. Geant4 physics reference manual. <https://geant4-userdoc.web.cern.ch/UsersGuides/PhysicsReferenceManual/html/index.html>
42. V. Kudryavtsev, Muon simulation codes MUSIC and MUSUN for underground physics. *J. Phys. Commun.* **180**, 339–346 (2009). <https://doi.org/10.1016/j.cpc.2008.10.013>. [arXiv:0810.4635](https://arxiv.org/abs/0810.4635)
43. Experimental Nuclear Reaction Data (EXFOR). <https://www-nds.iaea.org/exfor/>
44. DARWIN Collaboration, F. Agostini et al., Erratum to: Sensitivity of the DARWIN observatory to the neutrinoless double beta decay of  $^{136}\text{Xe}$ . *Eur. Phys. J. C* **83**, 996 (2023). <https://doi.org/10.1140/epjc/s10052-023-12036-2>
45. XENON Collaboration, E. Aprile et al., Search for new physics in electronic recoil data from XENONnT. *Phys. Rev. Lett.* **129**, 161805 (2022). <https://doi.org/10.1103/PhysRevLett.129.161805>. [arXiv:2207.11330](https://arxiv.org/abs/2207.11330)
46. KAMLAND-ZEN Collaboration, S. Abe et al., Measurement of cosmic-ray muon spallation products in a xenon-loaded liquid scintillator with KamLAND. *Phys. Rev. C* **107**, (2023). <https://doi.org/10.1103/PhysRevC.107.054612>, 054612. [arXiv:2301.09307](https://arxiv.org/abs/2301.09307)